



JES FOCUS ISSUE ON MATHEMATICAL MODELING OF ELECTROCHEMICAL SYSTEMS AT MULTIPLE SCALES IN HONOR OF JOHN NEWMAN

## Mesoscale Effective Property Simulations Incorporating Conductive Binder

Bradley L. Trembacki,<sup>\*[z](#)</sup> David R. Noble, Victor E. Brunini, Mark E. Ferraro,<sup>\*</sup> and Scott A. Roberts<sup>\*</sup>

Sandia National Laboratories, Albuquerque, New Mexico 87185-0840, USA

Lithium-ion battery electrodes are composed of active material particles, binder, and conductive additives that form an electrolyte-filled porous particle composite. The mesoscale (particle-scale) interplay of electrochemistry, mechanical deformation, and transport through this tortuous multi-component network dictates the performance of a battery at the cell-level. Effective electrode properties connect mesoscale phenomena with computationally feasible battery-scale simulations. We utilize published tomography data to reconstruct a large subsection (1000+ particles) of an NMC333 cathode into a computational mesh and extract electrode-scale effective properties from finite element continuum-scale simulations. We present a novel method to preferentially place a composite binder phase throughout the mesostructure, a necessary approach due difficulty distinguishing between non-active phases in tomographic data. We compare stress generation and effective thermal, electrical, and ionic conductivities across several binder placement approaches. Isotropic lithiation-dependent mechanical swelling of the NMC particles and the consideration of strain-dependent composite binder conductivity significantly impact the resulting effective property trends and stresses generated. Our results suggest that composite binder location significantly affects mesoscale behavior, indicating that a binder coating on active particles is not sufficient and that more accurate approaches should be used when calculating effective properties that will inform battery-scale models in this inherently multi-scale battery simulation challenge.

© The Author(s) 2017. Published by ECS. This is an open access article distributed under the terms of the Creative Commons Attribution Non-Commercial No Derivatives 4.0 License (CC BY-NC-ND, <http://creativecommons.org/licenses/by-nc-nd/4.0/>), which permits non-commercial reuse, distribution, and reproduction in any medium, provided the original work is not changed in any way and is properly cited. For permission for commercial reuse, please email: [oa@electrochem.org](mailto:oa@electrochem.org). [DOI: [10.1149/2.0601711jes](https://doi.org/10.1149/2.0601711jes)] All rights reserved.



Manuscript submitted April 20, 2017; revised manuscript received June 28, 2017. Published July 26, 2017. *This paper is part of the JES Focus Issue on Mathematical Modeling of Electrochemical Systems at Multiple Scales in Honor of John Newman.*

Lithium-ion batteries (LIB) have established themselves as a leading form of mobile energy storage, especially for consumer devices such as phones, laptop computers, and electric vehicles. LIBs consist of anode, separator, and cathode materials sandwiched between current collectors, with the anode and cathode typically being composite materials consisting of electrochemically active material particles, a polymeric binder, and conductive additives such as carbon. Combining and processing these components forms a porous electrode whose void space is then filled with liquid electrolyte. Typical commercial LIBs contain graphite as the anode active material and lithium insertion compounds like  $\text{LiCoO}_2$  (LCO) or  $\text{LiNi}_x\text{Mn}_y\text{Co}_{1-x-y}\text{O}_2$  (NMC) for the cathode active material. Secondary electrode components typically include a polyvinylidene fluoride (PVDF) polymeric binder, which holds active material particles together, along with carbon black to increase electrical conductivity.

Due to the widespread consumer usage of LIBs, especially as electric vehicles and their associated infrastructure become more prevalent, there is significant motivation to improve our understanding of their behavior and performance.<sup>1</sup> While a large portion of battery research observes and models battery behavior from a cell or battery-pack level,<sup>2–4</sup> the physical phenomena governing the battery operation take place at the mesoscale (particle-scale). At the mesoscale, electrochemical reactions occur on active material particle surfaces and ions/electrons undergo transport through the tortuous bi-continuous network formed by the constituent phases. Additionally, active materials typically experience a volumetric expansion/contraction with changes in lithiation, resulting in mechanical deformation and significant stress generation throughout the electrode.<sup>5</sup> This can affect the electrochemical performance by damaging the particle network.<sup>6–13</sup> While these mesoscale phenomena have significant effects on battery behavior, they are not fully understood, chiefly due to the difficulty in observing them during a transient battery charge/discharge.

Cell-level battery simulations must make simplifying assumptions about these phenomena and the particle-scale geometry in or-

der to be computationally feasible. Effective properties intended to represent a homogenized or volume-averaged electrode and simplifications like Bruggeman's formula are typically used.<sup>4,14,15</sup> Complexly shaped mesoscale geometrical features like electrochemically active surface area and the inherently tortuous pathways for electric/ionic/thermal conduction through the various constituent phases must be accurately captured to obtain realistic effective electrode-scale properties. This disconnect has resulted in a significant effort to develop mesoscale modeling and simulation capabilities within the battery modeling field.<sup>16–19</sup> Recent advancements in mesoscale imaging techniques have enabled detailed visualization of complex electrode mesostructures,<sup>20–32</sup> allowing modeling efforts to progress to real electrode morphologies.<sup>20,27,33–42</sup>

To bridge the gap between mesoscale and cell-level simulations, efforts have been made to extract electrode-scale properties from mesoscale reconstructions.<sup>43–47</sup> These effective properties represent the material property value for a homogenized volume-averaged treatment of the composite electrode and are necessary to feasibly solve full-battery simulations. The properties can be extracted from mesoscale simulation tools by considering a representative volume element (RVE) which contains a sufficient amount of composite material to be representative of the bulk electrode.<sup>48,49</sup>

Despite the advancements in imaging, there has been noticeable difficulty in resolving the location of all phases within the mesostructure. Specifically, the inability to distinguish PVDF, carbon, and void from each other<sup>23,50,51</sup> when using X-ray tomography has resulted in the omission of the PVDF and carbon black phases in many of the modeling studies referenced above. Neglecting them altogether results in a mesostructure with an artificially high porosity and low electrolyte tortuosity. Additionally, carbon additives are included to yield electrodes with sufficient electrical conductivity, making it likely that neglecting to resolve the location of carbon within the mesostructure has a significant effect on electrical conduction simulation accuracy. To address this issue, some recent efforts have been made to segment individual phases in Li-ion battery cathodes<sup>21,22,52</sup> using electron microscopy, but these are limited to relatively small domain sizes when compared to X-ray tomography. This could mean that the scanned

<sup>\*</sup>Electrochemical Society Member.  
E-mail: [btremba@sandia.gov](mailto:btremba@sandia.gov)

subdomain is not representative of the bulk, yielding misleading properties. To account for the lack of information in larger tomography image datasets, some studies have assumed the morphology of a composite binder phase (PVDF + carbon black). Some researchers assume a thin coating of binder on active electrode particles with a focus on stress simulation,<sup>17,39,53,54</sup> while others introduce more complex composite binder morphologies such as agglomerates/clusters and fibers/chains while focusing on electrode transport metrics such as conductivity and tortuosity.<sup>44,47,51</sup> While some electrode imaging shows binder distributed throughout the void space,<sup>55,56</sup> some recent electrode imaging suggests that binder concentrates into spaces between particles, forming pendular rings due to particle surface wetting and capillary forces during the drying process<sup>57,58</sup> and can migrate throughout the electrode during the drying process.<sup>59</sup>

In this study, we address imaging limitations and the interest in effective electrode-scale properties by comparing electrode-scale properties from simulations on mesostructure reconstructions that consider various composite binder phase placement approaches. We are predominantly interested in effective transport properties (electrical/ionic/thermal conductivity), but also investigate geometric parameters and internal stress metrics. Traditionally, a large focus has been placed on the cathode as it is often the limiting factor in battery performance, therefore we focus here on the cathode material LiNi<sub>1/3</sub>Mn<sub>1/3</sub>Co<sub>1/3</sub>O<sub>2</sub> (NMC333), which we refer to as NMC throughout paper. Both the models used to simulate mesoscale physical phenomena and the numerical methods used to generate mesostructural meshes are presented. We highlight several important NMC material properties that are sensitive to the amount of lithium stored in the NMC particles (mechanical swelling, electrical conductivity) and the effect that lithiation-induced particle swelling has on composite binder conductivity due to compressively straining it. These methods and material behaviors are used to compare several composite binder location representations to scenarios where composite binder is neglected to study the effects on electrode-scale effective properties as a function of NMC state of charge.

### Physical Models and Electrode-Scale Effective Properties

Our aim is to compare performance properties of various mesostructure and composite binder reconstructions. Here we present the physical phenomena simulated along with the metrics used to evaluate the particle-bed reconstructions. In many cases, these metrics are effective electrode-scale properties that can be used in large-scale cell-level simulations.

**Surface area.**—While electrochemical simulations are outside the scope of this study, we can use geometric information such as active particle surface area as an indicator of electrochemical performance. For a given discharge current, a larger particle-electrolyte interface area results in a reduced lithium ion flux per unit area. A reduced current density corresponds to reduction in lithium gradients within the particles, allowing for increased electrode utilization (capacity), and therefore making particle surface area a valuable electrode metric. Since we are explicitly resolving the composite binder phase, several interfacial areas will exist. Although we treat the composite binder phase as a solid in this study, it may be ionically conductive due to porosity.<sup>47,60</sup> This indicates that particle-binder interface area may be relevant to electrochemistry in addition to particle-electrolyte interface area.

**Transport.**—Along with electrochemistry, transport phenomena largely govern electrode performance at the mesoscale. As discussed in the introduction, a main motivation for reconstructing detailed electrode scans and performing mesoscale simulations is to accurately capture the pathways for ion/electron/thermal transport and extract homogenized electrode-scale effective material properties. We focus on evaluating four effective transport properties across the electrode reconstructions: effective electrical conductivity,  $\sigma^{eff}$ ; tortuosity,  $\tau$ ;

effective ionic conductivity,  $\kappa^{eff}$ ; and effective thermal conductivity,  $k^{eff}$ .

In general, we model conduction through the domain by solving for steady-state conservation,

$$\nabla \cdot \mathbf{J}_k = 0, \quad [1]$$

where  $\mathbf{J}_k$  is the generic flux vector. When solving for electrical conduction,

$$\mathbf{J}_{elec} = -\sigma_i \nabla \phi, \quad [2]$$

where  $\phi$  is electric potential and  $\sigma_i$  is the electrical conductivity of the various constituent phases ( $i$ ). Similarly, ionic conductivity is considered by solving steady state conservation (1) where the flux of interest is ionic flux,

$$\mathbf{J}_{ionic} = -\kappa_i \nabla \phi, \quad [3]$$

and  $\kappa_i$  is ionic conductivity of each phase, which is considered to be zero for all materials other than the electrolyte. As in the remainder of the paper, effects due to concentration gradients that may form during high-rate charge/discharge are neglected, resulting in the simplified ionic flux expression in (3). Lastly, we consider thermal transport by solving the steady state heat diffusion equation, which equates to (1) conserving a heat flux defined as

$$\mathbf{J}_{heat} = -k_i \nabla T, \quad [4]$$

where  $k_i$  is thermal conductivity of each phase and  $T$  is temperature.

In all three cases, a potential difference is applied across the electrode by applying Dirichlet (uniform potential) boundary conditions on the in-plane boundaries (parallel to current collector) and applying symmetry boundary conditions on the other four boundaries. The effective electrical conductivity can be calculated by assuming that the computational domain is a single homogeneous material and applying Ohm's Law:

$$\sigma^{eff} = \frac{-J_{elec}}{(\phi_1 - \phi_2)/L} \quad [5]$$

where  $J_{elec}$  represents current density in the direction of the voltage difference,  $\phi_1 - \phi_2$  is the voltage difference, and  $L$  is the distance between between the  $\phi_1$  and  $\phi_2$  Dirichlet boundaries.  $J_{elec}$  is obtained from

$$J_k = \frac{\int_S \mathbf{n} \cdot \mathbf{J}_k dS}{\int_S dS}, \quad [6]$$

where  $\mathbf{n}$  is the normal vector of the Dirichlet boundary surface  $S$ .  $\sigma^{eff}$  is likely to be dominated by the conductive composite binder phase with some contributions from the moderately conductive NMC active particle phase.

The effective ionic conductivity,  $\kappa^{eff}$ , is calculated similarly to (5) by considering total ion flux at the Dirichlet boundary as

$$\kappa^{eff} = \frac{-J_{ionic}}{(\phi_1 - \phi_2)/L} \quad [7]$$

where  $J_{ionic}$  is again calculated using (6). Since ionic conduction is limited to the void/electrolyte phase, electrolyte tortuosity can be calculated with

$$\tau = \frac{\kappa_e \varepsilon_e}{\kappa^{eff}}, \quad [8]$$

where  $\kappa_e$  is the intrinsic ionic conductivity of the electrolyte, and  $\varepsilon_e$  is the porosity (ratio of electrolyte volume fraction to total volume).<sup>61,62</sup> Tortuosity is an important electrode property, especially at high power densities, as it dictates how easily lithium ions can traverse the porous electrode.

Analogously to the electrical properties discussed above, effective thermal conductivity is extracted by obtaining a thermal heat flux,  $J_{heat}$ , across the boundary with (6) and using Fourier's Law,

$$k^{eff} = \frac{-J_{heat}}{(T_1 - T_2)/L}, \quad [9]$$

where  $T_1 - T_2$  is the temperature difference imposed across the length  $L$  of the domain. The noticeable difference between  $k^{eff}$  and the effective electronic/ionic properties is that all phases are thermally conductive to some degree and will therefore all participate in heat conduction across the electrode, ultimately impacting  $k^{eff}$ . Effective thermal conductivity plays a large role in how efficiently the composite cathode can dissipate heat generated during charge/discharge.

**Mechanics.**—Mechanics within the mesostructure are of interest here due to their impact on the transport physics previously discussed. In addition, mechanical phenomena likely play a significant role in battery cycle life and electrode degradation.<sup>7,63,64</sup> In these simulations, mechanical deformation of the composite cathode phases is considered to be quasi-static and is governed by the conservation of linear momentum,

$$\nabla \cdot \sigma = 0, \quad [10]$$

where  $\sigma$  is the Cauchy stress tensor. Here, we consider two components of the stress: a linear-elastic response and lithiation-induced swelling in the NMC phase. We approach the lithiation strain analogously to Vegard's law<sup>65–67</sup> and have detailed this approach previously.<sup>38</sup> We assume deformation in the small strain limit and thus the constitutive response takes the form

$$\sigma = \mathbb{C}_i : (\epsilon - \beta \Delta C_{Li}), \quad [11]$$

where  $\mathbb{C}_i$  is the fourth-order elasticity tensor,  $\epsilon$  is the small strain tensor, and  $\beta \Delta C_{Li}$  represents the lithiation-induced swelling strains within NMC where  $\Delta C_{Li}$  is a simple lithium concentration difference from the reference state of  $Li_{0.5}Ni_{1/3}Mn_{1/3}Co_{1/3}O_2$ . The second-order tensor  $\beta$  is a material property defined by  $\beta = \epsilon_{lith} / \Delta C_{Li}$  where  $\epsilon_{lith}$  is the lithiation-induced strain tensor. While recent studies suggest the mechanical behavior may be much more complicated than this,<sup>68,69</sup> the current approach allows a first look at the mechanical effects.

Solving the conservation equation yields stress and strain fields throughout the computational domain, allowing for comparison between various mesostructures. Strain values are useful when considering strain-dependent material properties. Using the stress tensor field, we extract two scalar stress fields that facilitate an understanding of the stress environment experienced by the NMC particles. The first is the von Mises stress ( $\sigma_v$ ), which is typically used as an indicator of stress state and to calculate a material's yield criterion. The von Mises stress field is defined by

$$\sigma_v = \sqrt{\frac{3}{2} s_{ij} s_{ij}}, \quad [12]$$

where  $s_{ij}$  are components of the stress deviator tensor,  $\sigma^{dev}$ . It is likely that high stress states could lead to particle fracture and reduced electrode performance,<sup>70</sup> making the von Mises stress a useful metric.

The second scalar stress field metric considered is the maximum shear stress,

$$\tau_{max} = \frac{1}{2} |\sigma_1 - \sigma_3|, \quad [13]$$

where  $\sigma_1$  and  $\sigma_3$  are the principal stresses. Maximum shear stress may be of interest when considering particle-particle separation due to swelling.

## Numerical Methods

We begin by presenting the methods used to generate a computational mesh that represents a cathode particle bed mesostructure composed of NMC active material particles and a non-active region from tomography imaging data. That method is then extended to include several approaches that add additional NMC material or a composite binder phase to account for the inability to distinguish between non-

active materials (binder, conductive additive, and void) in the imaging data.

**Image reconstruction and mesh generation.**—As discussed in Ref. 23, various tomography techniques exhibit a trade-off between image resolution and domain size. High resolution scanning electron microscopy (SEM) imaging indicates that microscale NMC particles are typically spherical agglomerates of many nanoscale primary particles.<sup>23</sup> However, feasible 3D representations of electrode microstructures are limited in size when using SEM. In contrast, X-ray tomographic microscopy (XTM) is capable of imaging relatively large electrode volumes representing thousands of sufficiently resolved NMC secondary particles. However, the XTM imaging is not capable of resolving the surface details of the secondary particles, neglecting the nanoporosity and surface roughness resulting from the agglomerate nature of the particles. Additionally, it is not possible to distinguish between the various non-active material regions of carbon black, PVDF, and epoxy (pore/electrolyte) in these XTM images, which is true of many composite cathode image stacks in the literature. For now, we consider only two regions: active and non-active.

To investigate the role of composite binder within the mesostructure, we selected a cathode from the XTM data published by the Wood group at ETH Zurich,<sup>23</sup> which provides image stacks representing  $LiNi_{1/3}Mn_{1/3}Co_{1/3}O_2$  (NMC333) particle beds that are approximately  $700 \times 700 \times 70 \mu\text{m}^3$  in size. The electrode corresponding to a 92/4/4 wt% loading of NMC/Carbon Black/PVDF and a calendaring pressure of 600 bar was selected for this study. We chose to use XTM data due to the large sample volume spanning many thousands of NMC particles. Through a separate study, we determined that a large computational domain size is critical when treating the electrode subset as a representative volume element (RVE) that exhibits bulk properties. In contrast, property values obtained from small domain sizes spanning only a few particles can vary widely depending on location, resulting in a poor RVE.

Using the commercially available image processing software Avizo (FEI, Hillsboro, OR) along with the published image data where individual particles have been identified via grayscale pixel coloring, a 3D volume representation for each NMC particle was generated within Avizo. From each particle volume, a surface mesh can be generated and exported in a standard format, such as a standard tessellation language (STL) file. There are inherent errors introduced when reconstructing smoothed 3D geometries from pixelated image data. Furthermore, there is evidence that significant errors were introduced in the particle labeling process performed by Ebner et al.<sup>23</sup> A pixel count comparison between the binarized images and the images where individual particles have been identified and labeled shows a noticeable reduction in active material volume fractions after the labeling process. This is likely due to using a watershed method, which could result in decreased particle size by removing a single layer of voxels (each  $370 \text{ nm} \times 370 \text{ nm}$ ) from particle surfaces. To mitigate these errors and approximations, we confirm that the final volume fractions of active and non-active regions in our finite element mesh match the volume fractions calculated from the binarized images and reported in Ref. 23. This is accomplished by growing/offsetting each particle surface by 330 nm normal to the surface, a value that is consistent with the hypothesized source of the error.

Once a set of STL surface mesh files representing individual NMC particles has been extracted from the data, an interface-conformal computational mesh can be created by using the Conformal Decomposition Finite Element Method (CDFEM) within Sandia's SIERRA/Krino library.<sup>71</sup> Details on CDFEM theory have been published elsewhere,<sup>72,73</sup> but we summarize the process here for completeness. The process begins with the selection of a generic tetrahedral mesh that defines the bounds and spatial resolution of the computational domain and is referred to as the background mesh. The automated algorithm begins by converting each particle STL file into a level-set distance field representation ( $\phi$ ) on the background mesh, where  $\phi$  is a signed euclidean distance function with  $\phi = 0$

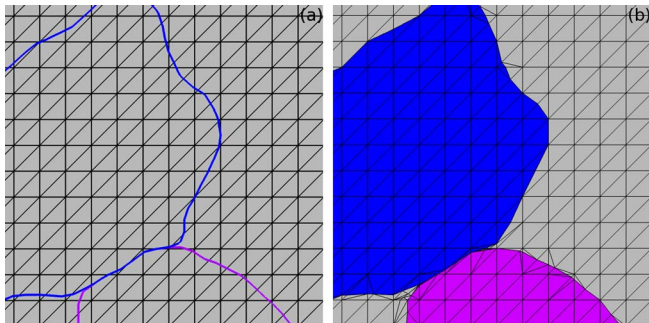


**Figure 1.** Illustration of the CDFEM process for a reconstructed electrode mesostructure, visualized in 2D for clarity. (a) Uniform background mesh (gray) with the overlaid colored curves depicting the particle surfaces. (b) Mesh after CDFEM decomposition, where the background mesh has been conformally split into a non-active phase (gray) and separate active particles phases (colored).

representing the particle surface and  $\varphi < 0$  representing the region inside the particle. CDFEM uses the level-set field to decompose the background mesh into an interface-conformal mesh. Elements are decomposed by adding nodes where the  $\varphi = 0$  surface intersects the edges of background mesh elements. The result is a connected 3D mesh that conforms to the interfaces defined by the original STL surfaces. By obtaining one STL file per particle, and therefore generating one level-set per particle, each particle surface can be conformed to individually and each particle can be treated separately in a finite element simulation. This distinction makes consideration of particle-particle contact phenomena or application of anisotropic material properties on a per-particle basis possible.

A visualization of the CDFEM process is provided in Figure 1. In Figure 1a, the uniform tetrahedral background mesh is colored gray, while the overlaid colored curves represent particle interfaces. The interfaces are not part of the mesh and are shown here to aid in visualization. The resulting mesh is shown in Figure 1b and demonstrates that the mesh has conformed to the particle interfaces by cutting the mesh elements that were intersected by a particle surface. A portion of the 3D mesh created by the CDFEM process is provided in Figure 2, where the active (NMC particles) and non-active (electrolyte+composite binder) phases are visualized separately.

In a separate study, we performed in-depth analysis of domain size effects and verification of spatial discretization error on reconstructions of the XTM data from Ebner et al.<sup>23</sup> The background mesh utilized in this study measures  $100 \times 100 \times 60 \mu\text{m}^3$  in size, which corresponds to a 1050-particle subset of the selected dataset and is shown in Figure 3. This size was chosen as it spans almost the entire thickness of the electrode ( $\sim 70 \mu\text{m}$ ) and  $100 \mu\text{m} \times 100 \mu\text{m}$  was determined to be a large enough lateral cross-section to reliably represent bulk properties. To keep discretization errors in effective properties less than 10% relative error while maintaining computational feasibility,

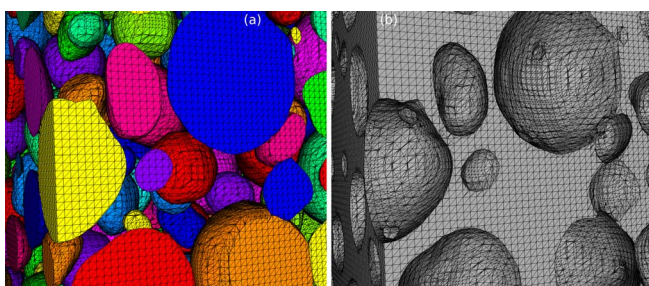


**Figure 2.** 3D visualization of the electrode computational mesh with (a) active NMC particles and (b) the non-active region (electrolyte + composite binder) visualized separately.

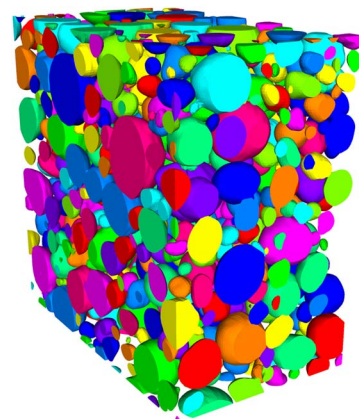


**Figure 3.** Reconstructed NMC cathode subset utilized throughout this study. The subset contains 1050 particles in a  $100 \times 100 \times 60 \mu\text{m}^3$  computational domain.

ity, a background mesh element size of  $0.75 \mu\text{m}$  was selected for this study, yielding computational meshes composed of approximately 20 million tetrahedral elements. We utilize the Galerkin finite-element method (FEM) within the SIERRA/Aria multi-physics simulation module to solve the governing equations presented.<sup>71</sup> Each set of physics (mechanical, thermal, electrical, ionic) is solved separately using Newton-Raphson nonlinear iterations combined with an algebraic multi-level preconditioned GMRES iterative linear solver. The mechanics simulation is performed first due to the strain-dependent composite binder conductivity relationship considered in our study.

**Composite binder representations.**—In order to account for the previously discussed limitations in distinguishing the composite binder from pores/electrolyte in experimental image data, several approaches for achieving the correct electrode porosity are considered for comparison. We treat the composite binder as a solid, therefore the correct electrode porosity (volume fraction of electrolyte) can be expressed as

$$\varepsilon_e = 1 - \varepsilon_{NMC} - \varepsilon_{NMC} \left[ \left( \frac{x_C}{100 - x_C - x_{PVDF}} \right) \left( \frac{\rho_{NMC}}{\rho_C} \right) + \left( \frac{x_{PVDF}}{100 - x_C - x_{PVDF}} \right) \left( \frac{\rho_{NMC}}{\rho_{PVDF}} \right) \right] \quad [14]$$

where  $\varepsilon_{NMC}$  is the volume fraction of active material extracted from the imaging data, and density values of  $\rho_C = 2 \text{ g/cm}^3$ ,  $\rho_{PVDF} = 1.78 \text{ g/cm}^3$ , and  $\rho_{NMC} = 4.7 \text{ g/cm}^3$  are assumed for the carbon black, dry PVDF, and NMC, respectively.<sup>23</sup> Weight loading percentages of  $x_C = 4$  and  $x_{PVDF} = 4$  for the carbon black and PVDF secondary additives are taken from the experimental manufacturing details.<sup>23</sup> For this electrode sample and domain chosen, we obtain  $\varepsilon_{NMC} = 0.462$  from the binarized images resulting in a porosity value of  $\varepsilon_e = 0.438$ , which agrees with the reported values in the publication corresponding to the image data.<sup>23</sup>

**Approach 1: particle expansion.**—The simplest approach to obtain the correct porosity is to enlarge or swell each particle by a thickness that results in the correct porosity. This approach captures the correct porosity, but artificially adds more active material than the raw images indicate. When choosing this route, one must decide how to account for the effects of the composite binder that is being neglected. For this study we assume that the expanded NMC particles retain intrinsic NMC material properties. The comparison of the original scan reconstruction (“raw” mesostructure) and the expanded-particles mesostructure resulting in the correct porosity is shown in Figure 4. It is clear that some pore space has been replaced by active material, which decreases the porosity and enlarges conductive pathways.

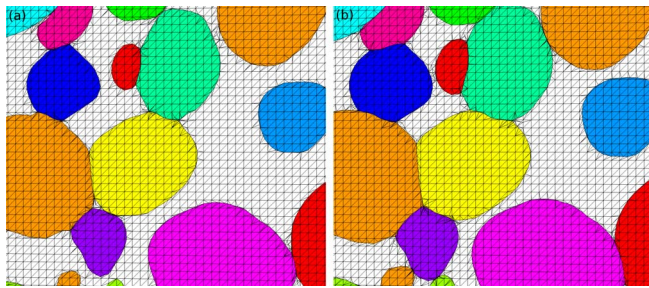


**Figure 4.** 2D visual comparison of a portion of (a) the raw mesostructure vs. (b) an expanded particles approach that results in the correct electrode porosity.

This particle expansion is achieved by offsetting each particle surface location by a constant distance normal to the surface. This numerically equates to

$$\varphi_{P,expanded,i} = \varphi_{P,i} - O, \quad [15]$$

where the offset,  $O$ , is applied to each individual particle level-set,  $\varphi_{P,i}$ , before the CDFEM mesh-cutting process. For this electrode sample, an expansion distance of  $O = 340$  nm resulted in the correct porosity value of  $\varepsilon_e = 0.438$ . Expanding the particles creates a scenario where two particles that were in contact are now defined as overlapping, meaning multiple level-set fields have negative values at the same location in space. Since the level-set fields represent distance functions, the overlap region is effectively smoothly bisected by assigning every point in space to the level-set whose value is the smallest (most negative).

**Approach 2: uniform composite binder coating.**—A similar yet more accurate approach is to apply a uniform coating of composite binder onto the particle surfaces. While this approach leaves no particle-electrolyte area for electrochemical reactions to occur, it is a commonly used approach due to its relatively straightforward implementation, especially in mechanically focused studies.<sup>17,39,53,54</sup> The coating thickness is again based on a calculation of the correct volume fractions from (14). While adding a third material phase to the computational domain may involve more effort, there is no artificial increase in active material capacity, which would cause erroneous performance simulations, especially in electrochemical simulations. Furthermore, the material properties of the composite binder can now be explicitly accounted for. Since the composite binder is significantly more conductive than the active NMC material, this will likely have a large impact on simulated electrical behavior. A visual representation of the binder coating approach is presented in 2D in Figure 5a and 3D in Figure 6a.

The binder coating mesh can be generated with CDFEM using several approaches. Here, we choose to use a segregated approach where we first perform CDFEM to produce a mesh that decomposes the domain into active particle regions and a non-active region followed

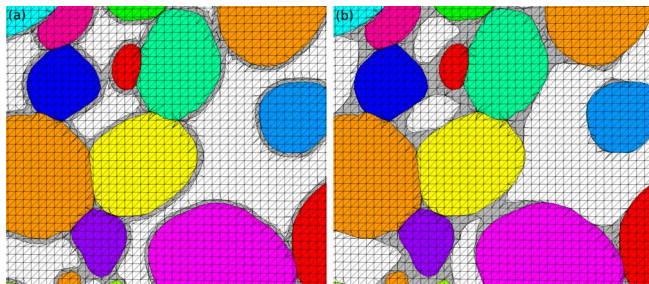


**Figure 5.** 2D visual comparison of (a) a composite binder coating approach vs. (b) a pendular ring composite binder approach that both result in the correct electrode porosity.

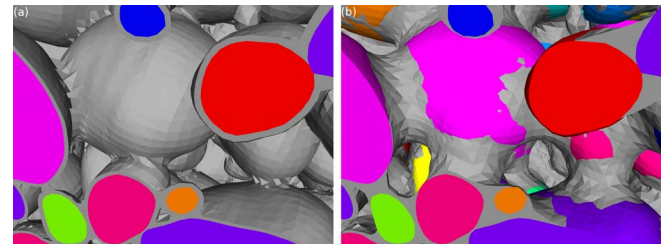


**Figure 6.** 3D visualization of NMC particles (colored) and composite binder (gray) for the two composite binder placement approaches.

by a subsequent CDFEM routine where the non-active region of the first mesh is decomposed into two regions: electrolyte and composite binder. While the decomposition into particles, composite binder, and electrolyte could all be performed in one step, the first step of the segregated process was already completed (referred to as “raw” mesostructure) and this approach guarantees that the particles are identically meshed when comparing different composite binder representations. To decompose the non-active region of the raw mesostructure mesh, a single level-set field representing composite binder is generated by reading all STL files defining particle surfaces and considering the combination as a single zero level. As in the expanded particles case, the level-set field representing the composite binder coating,  $\varphi_{B,coating}$ , is derived from offsetting before decomposition,

$$\varphi_{B,coating} = \varphi_{P,all} - O, \quad [16]$$

where  $O$  is the offset value and  $\varphi_{P,all}$  is the level-set distance field generated from the consideration of all particle level-sets at each point in the domain and is defined as

$$\varphi_{P,all} = \min(\varphi_{P,i}, \dots, \varphi_{P,N}) \quad [17]$$

where particle number index  $i$  ranges from 1 to the total number of particles,  $N$ . The non-active region is then decomposed into a composite binder phase ( $\varphi_{B,coating} < 0$ ) and an electrolyte phase ( $\varphi_{B,coating} > 0$ ). An offset value of  $O = 340$  nm again yields the correct electrode porosity, since adding a 340 nm coating of composite binder has the same effect on porosity as uniformly expanding each particle by that same distance.

**Approach 3: composite binder near particle contacts.**—As discussed in the introduction, imaging studies have suggested that the composite binder phase typically resides near the particle contacts forming pendular rings<sup>57</sup> that are hypothesized to form due to particle surface wetting combined with capillary transport during the drying process.<sup>74</sup> We have reproduced the image published by Jaiser et al.<sup>57</sup> in Figure 7 for comparison with our effort to mimic this structure in our computational domain. We again start from the raw mesostructure mesh previously decomposed into active and non-active regions, considering the non-active region to be our background mesh for this CDFEM process. First, a level-set is generated for each particle surface ( $\varphi_{P,i}$ ), followed by the generation of a single composite binder level-set constructed by evaluating

$$\begin{aligned} \varphi_{B,contacts} = \min & [( \varphi_{P,i} + O ) * ( \varphi_{P,j} + O ) \\ & - S, \dots, ( \varphi_{P,N} + O ) * ( \varphi_{P,N} + O ) - S ], i \neq j \end{aligned} \quad [18]$$

at each point in space, where particle number indexes  $i$  and  $j$  independently range from 1 to  $N$ ,  $O$  again denotes a level-set offset, and  $S$  is a non-physical size parameter that dictates the size of the “smooth bridge” created between particles. For each pair of particles, the particle level-sets are uniformly shrunk by offset  $O$ , multiplied together, and then grown by the product offset parameter  $S$ , which preferentially places composite binder in regions close to two particles. The effect of the offset and size parameters on two adjacent spherical particles is visualized in Figure 8.

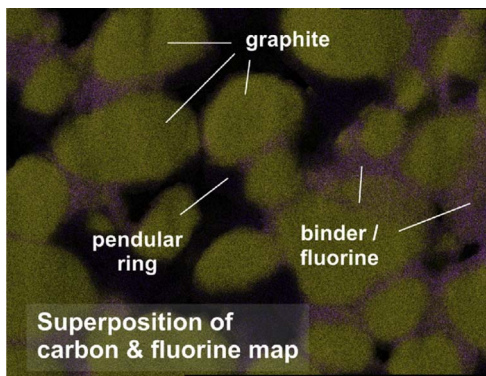


**Figure 7.** Experimental image reproduced from Jaiser et al.<sup>57</sup> that maps detailed morphology within an anode mesostructure, highlighting the presence of conductive binder near particle-particle contact regions and small gaps between particles. Reprinted from Journal of Power Sources, Vol 345, Jaiser et al., “Microstructure formation of lithium-ion battery electrodes during drying – An ex-situ study using cryogenic broad ion beam slope-cutting and scanning electron microscopy (Cryo-BIB-SEM)”, pps. 97–107, Copyright 2017, with permission from Elsevier.

It is important to note that many combinations of the parameters  $O$  and  $S$  could represent the correct volume fraction of composite binder while resulting in different morphologies with varying amounts of particle coverage. In the limit  $O = 0$ , the entire particle surface would be covered with binder, so a value that sufficiently moves the level-set zeros to reside within each particle needs to be used. However, such a scenario results in no binder phase, so the value of  $S$  is increased until the composite binder phase is sufficiently represented. Values of  $O = 970$  nm and  $S = 4.05 \times 10^6$  nm<sup>2</sup> were determined to yield the correct electrode porosity value while best resembling Figure 7, as visualized in Figure 6b. The two most important features are captured: there is sufficient binder near particle-particle contacts to allow for conduction, and binder does not fully coat the particles, removing the possibility of a conduction pathway that entirely bypasses the active material. We don't expect results to be highly sensitive to the exact  $S$  and  $O$  combination chosen, provided that  $O$  is sufficiently large ( $\sim 1$  μm) and  $S$  is increased to match the correct volume fraction.

It should also be noted that due to being composed of distance function products,  $\varphi_{B,contacts}$  is itself not a distance function. Since the mesh decomposition algorithms were developed assuming that level-sets are distance functions, a redistancing operation is performed on  $\varphi_{B,contacts}$  to convert it to a signed distance field while maintaining the same zero level. As in the composite binder coating case, the non-active phase from the raw mesostructure mesh is decomposed into composite binder and electrolyte, resulting in the finalized mesh with the correct volume fraction of composite binder preferentially placed near particle-particle contact regions.

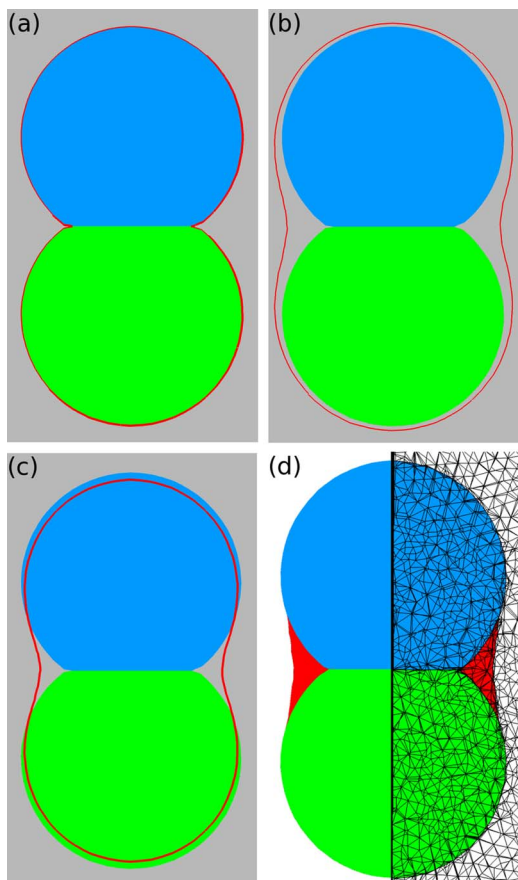


**Figure 8.** Visualization of the effect of parameters  $O$  and  $S$  in (18) on two synthetic particles denoted by subscript 1 and 2 (blue, green) and non-active region (gray) where the overlaid red line represents the equation (a)  $\varphi_1 * \varphi_2 = 0$  (b)  $\varphi_1 * \varphi_2 - S = 0$  (c)  $(\varphi_1 + O) * (\varphi_2 + O) - S = 0$ . The resulting geometry/mesh composite is shown in (d) where the non-active region in (a)–(c) (gray) has been decomposed into composite binder (red) and electrolyte (white).

*Approach 2a/3a: separating particles.*—Advanced element-mapping imaging techniques suggest that binder resides between active particles,<sup>57</sup> but the imaging techniques informing our mesostructure reconstruction process have a voxel resolution of 370 nm<sup>23</sup> and therefore may not be able to resolve particle-particle separation distances smaller than that resolution. To investigate the impact of this limitation, we recreate the two binder location approaches above (Approaches 2 and 3) but first place a 1/2 voxel (190 nm) composite binder interface layer between each pair of particles that are separated by a distance less than 190 nm. As this involves removing a small fraction of active material, the level-set describing the interface layer must be included in the initial decomposition along with the particle level-sets and is expressed as

$$\begin{aligned} \varphi_{B,interface} = \min [ & \max (\varphi_{P,i} - I, \varphi_{P,j} - I), \dots, \\ & \max (\varphi_{P,N} - I, \varphi_{P,N} - I) ], i \neq j \end{aligned} \quad [19]$$

where  $I$  is the composite binder interface thickness and  $i$  and  $j$  again span the range of  $N$  particles.  $\varphi_{B,interface}$  inherently overlaps particle level-sets, and the domain decomposition is handled as explained in the expanded particles method description. This algorithm is used in combination with the binder approaches discussed above, allowing comparisons between cases with and without an interface binder layer. The combination of this forced binder interface layer and the near-contacts binder approach on two spherical particles is presented visually in Figure 9 as an example.

## Material Properties

Here we focus on presenting the material properties included in our study that likely play a large role in determining electrode-scale effective properties. Lithiation-induced swelling and lithiation-dependent NMC electrical conductivity ( $\sigma_{NMC}$ ) are discussed first, followed by the introduction of a novel composite binder conductivity ( $\sigma_b$ ) approach where the value of  $\sigma_b$  is strain-dependent.

**NMC mechanical swelling and conductivity.**—NMC electrical conductivity ( $\sigma_{NMC}$ ) has been shown to have a very strong dependence on state of charge, as evidenced by the piecewise-linear reproduction of findings by Amin et al. shown in Figure 10a.<sup>75</sup> With such an extreme reduction in NMC conductivity at high lithium concentrations, the

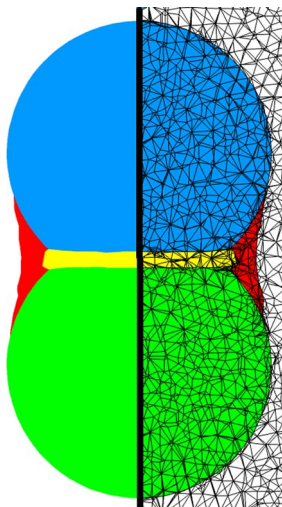


**Figure 9.** Composite visualization of the geometry and mesh resulting from the combination of the composite binder interface layer (yellow) and composite binder “smooth bridge” near particle contacts (red) on a synthetic two-particle (blue, green) domain.

high-conductivity composite binder will likely play a large role in electrical performance at those states of charge.

There have been several studies that aim to quantify how the lattice spacing parameters of a layered oxide crystal structure change when lithium insertion compounds lose/gain lithium.<sup>76,77</sup> These studies show that there is a small but measurable volume dependence on lithiation. Additionally, it is clear that this volume change is anisotropic, with the crystal structure shrinking in the in-plane or *a* directions while expanding in the out-of-plane or *c* direction. Although

the single-crystal strain is anisotropic, we consider the lithiation-induced volume change to be isotropic since the microscale NMC particles under consideration are typically agglomerates of many smaller NMC primary particles rather than single crystals.<sup>23</sup> A linear relationship between lithiation and crystal lattice unit cell volume was fit to the experimental study of NMC333 performed by Kam et al.<sup>76</sup> Due to an isotropic swelling assumption, the lithiation-dependent strain in each coordinate direction is equivalent and can be described by

$$\epsilon_{lith,xx} = \epsilon_{lith,yy} = \epsilon_{lith,zz} = \frac{1}{3}\epsilon_{lith,v} = 0.010279x - 0.00514 \quad [20]$$

where *x* represents the stoichiometric value of lithium in NMC and  $\epsilon_{lith,v}$  is lithiation-induced engineering volume strain relative to the assumed zero strain reference point where *x* = 0.5.  $\epsilon_{lith}$  is the lithiation-induced strain tensor, which is assumed to be a diagonal tensor with diagonal values of  $\epsilon_{lith,xx}$ ,  $\epsilon_{lith,yy}$ , and  $\epsilon_{lith,zz}$ . This relationship is plotted in Figure 10b and corresponds to a volume increase of 1.54% as NMC is lithiated from *x* = 0.5 to *x* = 1. Active particle swelling causes large stresses to form as the relatively stiff particles interact.<sup>33,39</sup> Furthermore, composite binder surrounding and between particles experiences compressive strains due to the particle swelling, which has recently been shown to impact its properties and is discussed in the next section. The lithiation-induced volume strain is treated analogously to a thermal expansion and its implementation is discussed in our physical models section.

**Strain-dependent composite binder conductivity.**—Recent experimental work<sup>78,79</sup> has determined that the electrical conductivity of the composite binder phase is strain-dependent, likely due to carbon particles/agglomerates being pushed into closer proximity when the composite binder is compressed. Using data from Grillet et al.<sup>79</sup>, we develop relationships for electrical conductivity as a function of engineering volume strain for both fresh and mechanically cycled composite binder films. In their study, composite binder films were swollen with electrolyte and then subjected to compressive strain/relaxation cycles while measuring electrical conductivity. We define “fresh” properties as measurements from the second strain cycle, while “cycled” properties correspond to measurements made after ~15 strain/relaxation cycles. There is a noticeable difference in conductive quality of the composite binder after strain cycling, a process which likely occurs during electrochemical cycling within the electrode mesostructure due to the expansion of the NMC particles upon lithiation. The best-fit linear relationships for conductivity are

$$\sigma_{b,fresh} = -17.3967\epsilon_v + 0.01593 \quad [21]$$

and

$$\sigma_{b,cycled} = -9.18767\epsilon_v + 0.001879 \quad [22]$$

in S/cm and are presented along with the experimental data points in Figure 11. Engineering volume strain,  $\epsilon_v$ , is defined as

$$\epsilon_v = \frac{V - V_0}{V_0} = \det \mathbf{F} - 1 \quad [23]$$

where  $\mathbf{F}$  is the deformation gradient obtained from the mechanical swelling simulation,  $V_0$  is the original unstrained volume, and  $V$  is the deformed volume resulting from the particle swelling simulation. A  $\det \mathbf{F}$  value and associated conductivity is calculated for each point in the composite binder phase following the mechanical swelling simulation and is provided to electrical conductivity simulations.

As the volume strain for a given element in the computational domain may exceed the range of experimental data used to determine the linear relationships, the conductivity vs. strain function is held constant outside of acceptable conductivity bounds. Any  $\epsilon_v$  values that are less than zero (location is in tension) are held to the unstrained conductivity value ( $\epsilon_v = 0$ ) due to lack of tensile strain versus conductivity relationship information. We bound the upper limit of conductivity to the manufacturer-specified intrinsic conductivity of the Denka acetylene black conductive additive used to make the composite binder

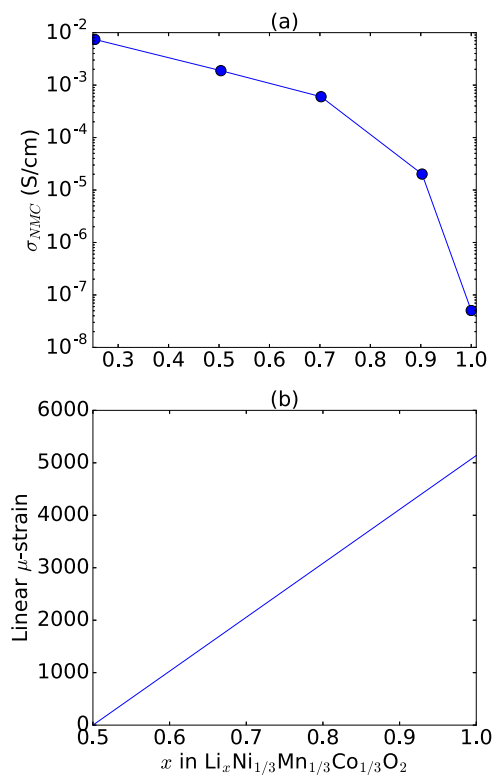


**Figure 10.** Lithiation-dependent NMC material properties included in simulations: (a) NMC electrical conductivity versus state of charge (lithiation)<sup>75</sup> and (b) Isotropic linear strain in NMC versus state of charge (lithiation)<sup>76</sup>.

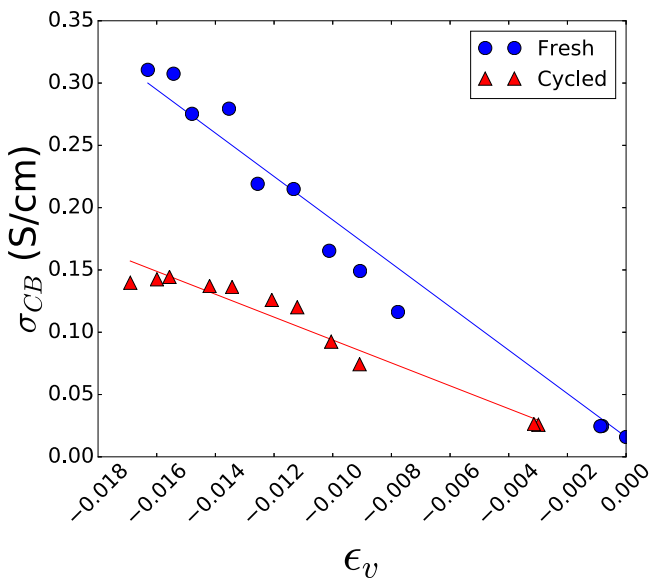


**Figure 11.** Electrical conductivity vs. volume strain for both fresh and mechanically cycled binder films swollen with electrolyte solution. The data points represent averages across 4 samples<sup>79</sup>, and the lines represent the best-fit linear relationships used in our simulations and described by (21) and (22).

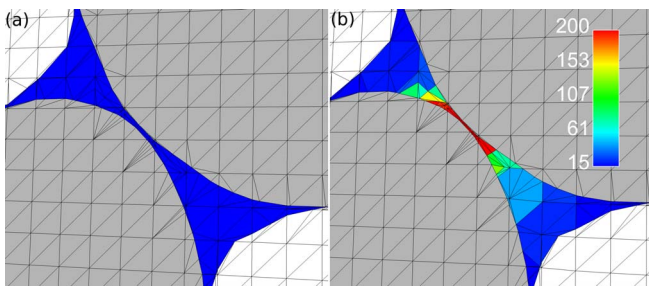


**Figure 12.** Comparison of (a) unstrained vs. (b) swollen NMC particles. Particle swelling compresses the composite binder, increasing its conductivity in accordance with (21) and (22). The particles (gray) and electrolyte (white) are included for clarity, and the color map represents composite binder electrical conductivity in S/m.

films,  $\sigma_C = 5 \text{ S/cm}$ . Figure 12 presents a visualization of the effect of particle swelling on composite binder conductivity, where an increase in lithiation corresponds to compression of the composite binder and therefore an increase in electrical conductivity.

While the relationship between compressive strain and composite binder electrical conductivity is important, the magnitude of the conductivities reported in Ref. 79 are significantly lower than the values of  $\sim 1 \text{ S/cm}$  reported in the literature.<sup>80,81</sup> One possible cause for this is that lateral layers of carbon black aggregates could form when making the film, while conductivity was measured in the vertical direction. We acknowledge this discrepancy by comparing both the linear fits discussed here as well as an upper-bound scenario where the composite binder conductivity vs. strain functions are increased by an order of magnitude, but are still capped at 5 S/cm.

**Material properties summary.**—We conclude this section by tabulating relevant material properties in Table I. A value for ionic conductivity in the electrolyte,  $\kappa_e$ , is omitted as the metric of interest when calculating tortuosity is relative ( $\kappa^{eff}/\kappa_e$ ) and therefore an arbitrary value of  $\kappa_e$  was used for those simulations. We were unable to locate an intrinsic thermal conductivity value for any formulation of NMC material in the literature, so a  $k$  value for LCO material is used.<sup>82</sup>

## Results and Discussion

Geometric and physical metrics extracted from mesoscale simulations are presented here. Throughout this section, we use abbreviated names for the mesostructures detailed in the image reconstruction and mesh generation section above. The original image reconstruction, where there is simply an active (NMC) and non-active segmentation (electrolyte), is referred to as *raw* (Figure 4a). The case where the particles are expanded to yield the correct porosity, while still neglecting the presence of composite binder is denoted as *expanded* (Approach 1, Figure 4b). The two composite binder representation cases are referred to as *coating* and *contacts*, corresponding to Approach 2 and Approach 3 visualized in Figure 5a,5b, respectively. We assume there is no particle-particle contact resistance and no binder interface layer is forced between particles with the exception of the study specifically focusing on the addition of a thin interface layer separating all particle contacts. Properties that are sensitive to lithiation are presented as curves against degree of cathode lithiation, while lithiation-insensitive metrics are presented as bar charts. We begin by discussing the particle surface areas, followed by the stresses generated within the mesostructure due to NMC swelling. Next, we discuss the electrode's effective electrical conductivity, ionic conductivity (tortuosity), and thermal conductivity.

**Surface area.**—Particle surface area is an important metric when considering electrochemistry within the electrode and is typically represented in battery-scale simulations through the specific surface area,  $a$ , which is the ratio of particle surface area to particle volume. While  $a$  is typically approximated by assuming a packed bed of spherical particles,<sup>83</sup> here we report specific surface areas of the real electrode mesostructure reconstructions in Figure 13. Both particle-electrolyte ( $p-e$  Area) and particle-binder ( $p-b$  Area) interface areas are included. Expanding the particles increases surface area by  $\sim 6.2\%$  but also increases volume by  $\sim 20\%$ , resulting in the reduced  $a$  value reported. By definition, we see that the coating case converts all particle surface area to particle-binder interface area. Interestingly, our choice of parameters results in  $\sim 80\%$  of the particle surface being covered with composite binder in the contacts case. This is a useful finding, as an accurate representation of the mesostructure likely needs to distinguish  $p-e$  Area and  $p-b$  Area for use in electrochemical simulations.

For comparison to traditional approximations, we can calculate the average spherical particle radius of this electrode by using the particle size distribution (PSD) information provided with the image data by Ebner et al.<sup>23</sup> An average particle radius approach is very typical in macroscale simulation efforts.<sup>4,15</sup> From the PSD volume value for each particle, we can calculate each particle's radius assuming it is spherical and obtain an average particle radius of  $R_p = 2.878 \mu\text{m}$  and a corresponding specific surface area of  $a = 3/R_p = 1.04 \mu\text{m}^{-1}$ . This approximated  $a$  value is 81% higher than our observed value of  $0.576 \mu\text{m}^{-1}$  largely due to reducing the particle size distribution to a single radius and not accounting for particle-particle contact area and

**Table I.** Summary of material properties.

Property	Symbol	Units	NMC	Composite Binder	Electrolyte
Electrical conductivity	$\sigma$	S/cm	Figure 10a	Figure 11	—
Thermal conductivity	$k$	W/m·K	4.0 <sup>82</sup>	0.2 <sup>84,85</sup>	0.16 <sup>86</sup>
Young's modulus	$E$	Pa	$139 \times 10^9$ <sup>87</sup>	$70 \times 10^6$ <sup>79</sup>	—
Poisson's ratio	$\nu$	—	0.2 <sup>66</sup>	0.34	—

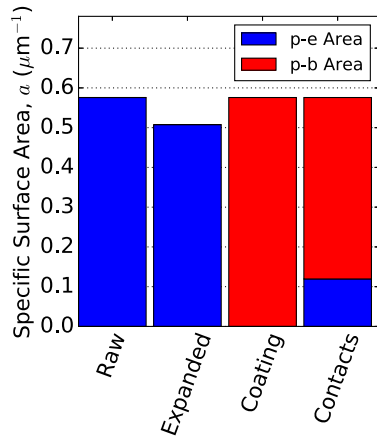


**Figure 13.** Specific surface area totals for each mesostructure where *p* – *e* Area corresponds to particle surface in contact with electrolyte while *p* – *b* Area is the contact between particle and composite binder.

non-spherical particles. If we instead use the individual particle radii and sum individual particle surface areas and volumes (again assuming spheres), the  $a$  value is  $0.604 \mu\text{m}^{-1}$ . This value is significantly closer ( $\sim 4.9\%$  error) to the value extracted from our mesostructure, despite not accounting for particle-particle contact or non-spherical particles, indicating that a full reconstruction into a 3D geometry may not be necessary to calculate volumes and surface areas for these NMC datasets if particle size distribution information is not averaged. In order to isolate the error due to a spherical particle assumption, we can include particle-particle contact area in the reconstruction  $a$  calculation. The value of  $a$  increases from  $0.576$  to  $0.597 \mu\text{m}^{-1}$ , resulting in a spherical assumption error of only  $\sim 1.2\%$  and indicating that neglecting particle-particle contact area introduces more error than assuming spherical particles. It is important to note that the discrepancy between idealized spherical surface area and truly available surface area becomes more significant with consideration of the composite binder phase blocking some portion of the particle surfaces, which may necessitate the examination of a 3D geometry reconstruction with strategically placed binder as we have done here.

**Mechanical stress.**—After mesh generation and geometry measurement, the next step in our process is to apply a uniform lithium concentration in all NMC particles and simulate the associated mechanical swelling. Since the boundaries of the composite electrode are fixed, this swelling generates significant stresses within the domain near particle-particle contact regions, as shown in Figure 14a. We note that since particle surface roughness is not captured in the reconstruction, surface stress values may be misrepresented here. We also acknowledge that while we are applying a uniform lithium concentration value, significant concentration gradients may be present within the NMC particles during high-rate battery operation. In Ref. 39, transient simulations similar to our steady-state simulations were performed for an LCO electrode mesostructure. They predict that the difference in maximum von Mises stress within the domain only changes 9% when comparing across charge rates of  $0.01\text{C}$  to  $10.0\text{C}$ , therefore we have neglected the transient effects here when comparing across binder geometries. We extract several representative metrics across lithiation states and present the results in Figure 15. The expanded case, having significantly more particle-particle contact than the other cases, shows significantly higher mean stress values ( $\sim 300\%$ ) due to the high NMC modulus. The cases with binder show slightly higher mean stresses than the raw mesostructure due to the replacement of a fluid with a solid, although the effect is small due to the relatively low modulus value of the composite binder.

The trend shown in the plot of maximum stresses is somewhat unexpected, as the expanded case, which exhibits the most particle-particle contact, shows the lowest maximum stress. However, this can

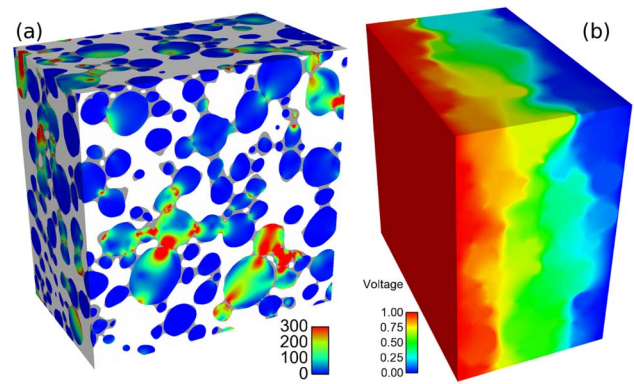


**Figure 14.** Example steady state fields resulting from a mechanics and effective electrical conductivity simulation for both (a) von Mises stress (MPa) in the NMC particle phase with electrolyte colored white and composite binder placed near particle contacts colored gray and (b) voltage.

be explained by the fact that sharp surface features act as stress concentrators, as explained by our previous efforts and in the literature.<sup>39,66</sup> Artificially expanding particles causes overlap in the particle level-set definitions which results in a relatively smooth interface between the two particles midway between the overlap. An example of this effect is shown in Figure 16 where the maximum stress value is lower when particles are expanded rather than barely touching.

**Electrical conductivity.**—Once the stress/strain response due to NMC swelling has been calculated, the strain-dependent binder conductivity field can be populated and simulation of electrical conduction is possible. A visualization of a typical resulting voltage field is presented in Figure 14b and the comparison of effective electrical conductivity considering several parameter permutations across lithiation states is provided in Figure 17. We consider both fresh (top row) and cycled (bottom row) composite binder properties. Due to the lower

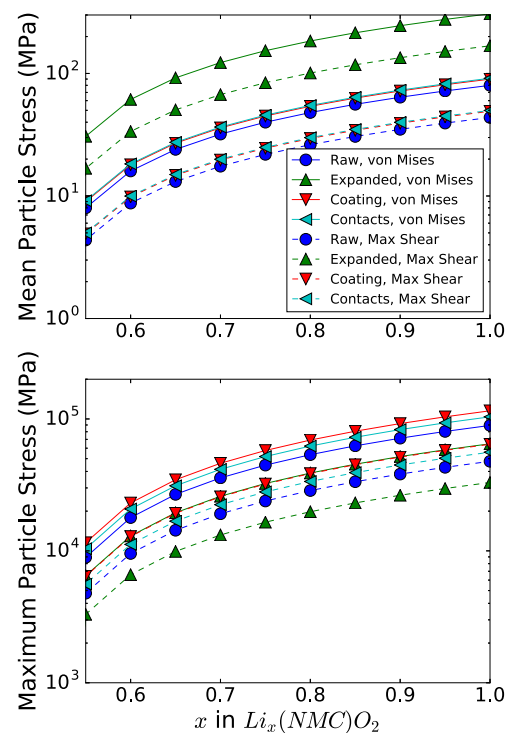


**Figure 15.** Maximum and mean stresses experienced by the NMC particles for all mesostructure representations. Both von Mises stress and maximum shear stress are displayed.

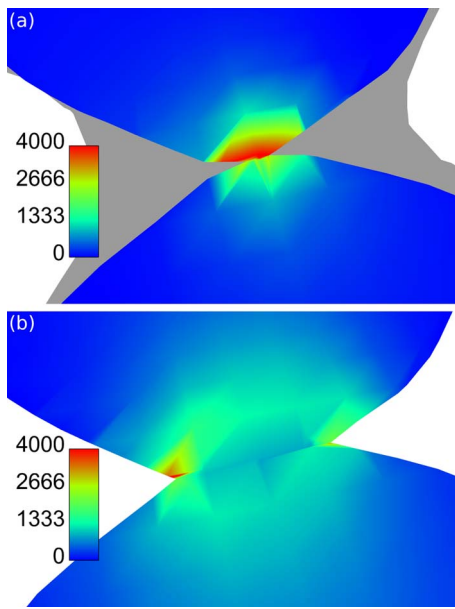


**Figure 16.** Comparison of von Mises stress field (MPa) on two mesostructure representations, (a) contacts and (b) expanded.

than expected magnitude of the published strain-dependent binder conductivity used in our study, we consider both the experimental values from<sup>79</sup> (left column) and the application of a 10x multiplier on the composite binder conductivity vs. strain relationship (right column). All four approaches are again represented, and the mesostructures that include composite binder have two lines each, corresponding to two

composite binder conductivity ( $\sigma_b$ ) field approaches: one that exhibits spatially-varying strain-dependence and one that assumes a uniform, constant value equal to the unstrained  $\sigma_b$  value. Since we consider the  $x = 0.5$  state of charge as the strain-free state, effective conductivity values for the strain-dependent and constant  $\sigma_b$  approaches are equivalent there.

For all binder geometries and conductivities considered, the effective electrical conductivity of the composite electrode,  $\sigma^{eff}$ , is higher when binder is present in the domain. This is not surprising, as one role of the composite binder is to improve conductivity. The data presented in Figure 10a demonstrates a severe decrease in NMC conductivity as lithiation increases, causing most of the  $\sigma^{eff}$  trends to likewise exhibit a decrease with increasing lithiation. The near-zero  $\sigma^{eff}$  values at higher lithiation states for the two cases without binder are especially noteworthy and highlight that composite binder effects cannot be neglected.

The dotted lines representing a constant value for  $\sigma_b$  all decrease with lithiation, as expected due to decreasing  $\sigma_{NMC}$  being the sole lithiation-dependent intrinsic  $\sigma$  value. However, when strain-dependent composite binder conductivity is considered (solid lines), there is a competition between decreasing  $\sigma_{NMC}$  and increasing  $\sigma_b$  due to increasing compressive binder strain as lithiation increases. Depending on the magnitude of  $\sigma_b$  considered, we see that competition result in different behaviors, with  $\sigma^{eff}$  even increasing with lithiation in some cases. Neglecting strain-dependent  $\sigma_b$  properties results in up to a 50% reduction in predicted  $\sigma^{eff}$ , indicating that it is a significant property to include in future simulation efforts.

In subplots (a), (c), and (d), there is a point where the coating  $\sigma^{eff}$  crosses the contacts  $\sigma^{eff}$ . At low lithiation states, the contacts case typically exhibits higher conductivity due to wider conductive pathways from one particle to the next. However, since binder is only placed near multi-particle regions, the particle phase must participate in most conductive pathways, making the  $\sigma^{eff}$  sensitive to  $\sigma_{NMC}$ . In contrast,

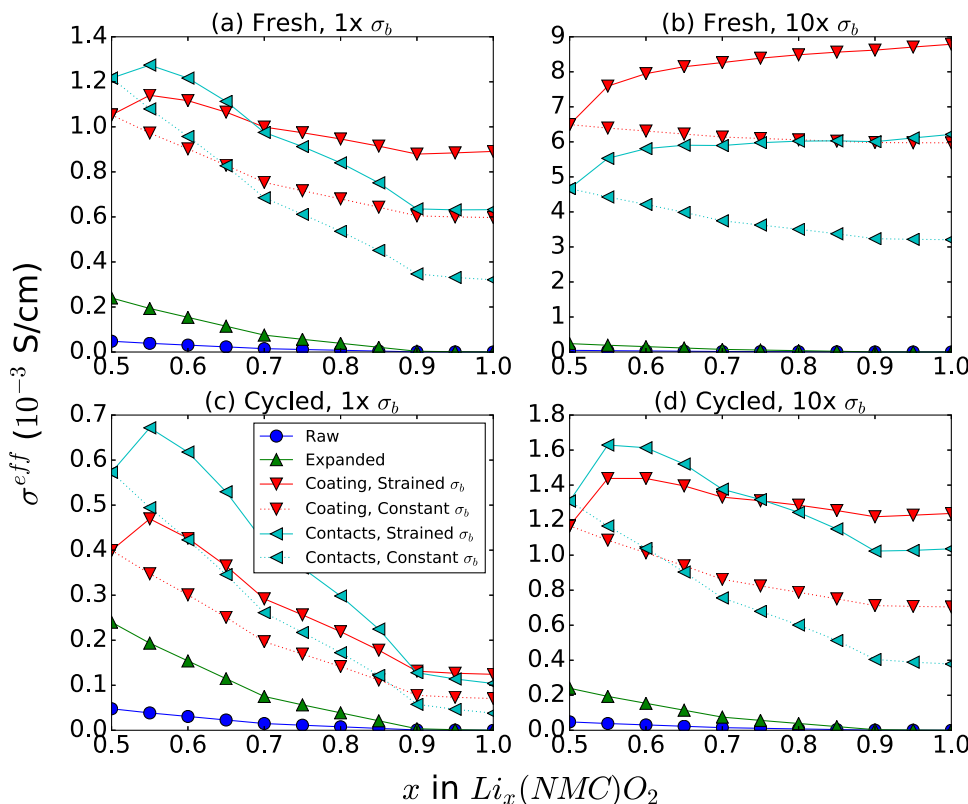


**Figure 17.** Effective electrical conductivity of the composite cathode for various mesostructure representations. Strained  $\sigma_b$  indicates that a locally strain-dependent composite binder conductivity field was used while Constant  $\sigma_b$  indicates that a single, constant  $\sigma_b$  value was used throughout the domain across all lithiation/strain states.

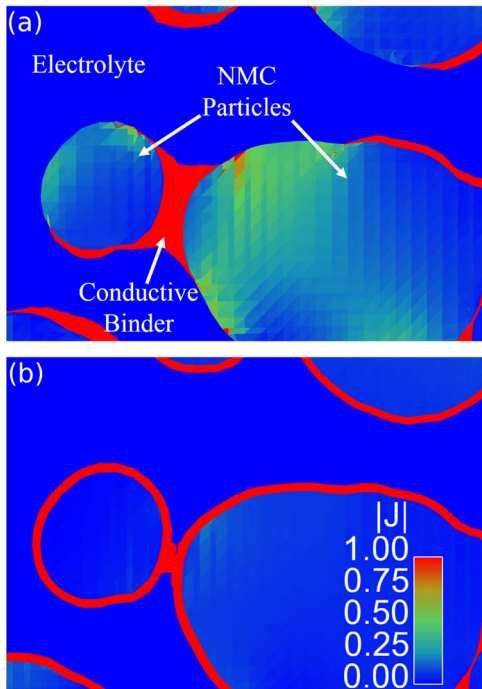


**Figure 18.** Comparison of current density magnitude on the two binder representations, (a) contacts and (b) coating, both with fresh binder, fully lithiated, highlighting the current flow through the NMC particles in (a) and the ability for current to bypass the particles in (b).

the  $\sigma^{eff}$  value for the coating case is less sensitive to decreasing  $\sigma_{NMC}$  because current can flow entirely through the composite binder phase from boundary to boundary. In general, this feature causes the contacts case to exhibit lower  $\sigma^{eff}$  values as the  $\sigma_b/\sigma_{NMC}$  ratio increases. Despite  $\sigma_{NMC}$  decreasing over 4 orders of magnitude from  $x = 0.5$  to  $x = 1.0$ , we see only a 10% decrease in the coating  $\sigma^{eff}$  in subplot (a) and an overall increase in coating  $\sigma^{eff}$  in both (b) and (d). A visual example of this effect is presented in Figure 18 where significantly higher current density through the NMC particle phase is necessitated by the contacts composite binder representation (Figure 18a), whereas the current flows nearly entirely through the composite binder in Figure 18b.

In Figure 19 we consider an additional approach for the  $\sigma_b$  value to evaluate the significance of spatial variance in the strain-dependent  $\sigma_b$  field. To achieve this, we compute a spatial mean value for the strain-dependent  $\sigma_b$  over the entire composite binder phase. The spatial means for each mesostructure and conductivity multiplier considered are presented in Figure 19a. In Figure 19b we compare  $\sigma^{eff}$  values for the spatially varying strain-dependent  $\sigma_b$  field to the uniform spatially averaged strain-dependent  $\sigma_b$  value for only one of the cases in Figure 17, as trends are similar across cases. This comparison emphasizes the importance of the incorporating the spatially-varying  $\sigma_b$  and shows that simply using an averaged uniform  $\sigma_b$  for the entire composite binder phase does not accurately capture the locally strain-dependent effects on  $\sigma^{eff}$ .

Overall, the results presented here indicate that inclusion of composite binder effects and the spatially varying strain-dependence of its electrical conductivity both have a significant impact on effective electrical conductivity. The two different binder location approaches also show significantly different behavior, indicating that a simple uniform binder coating representation does not sufficiently capture electrical transport through the composite structure, chiefly due to its ability to entirely bypass conduction through the NMC particle phase.

**Electrolyte tortuosity/ionic conductivity.**—Transport of lithium ions through the tortuous electrolyte-filled pore network is another

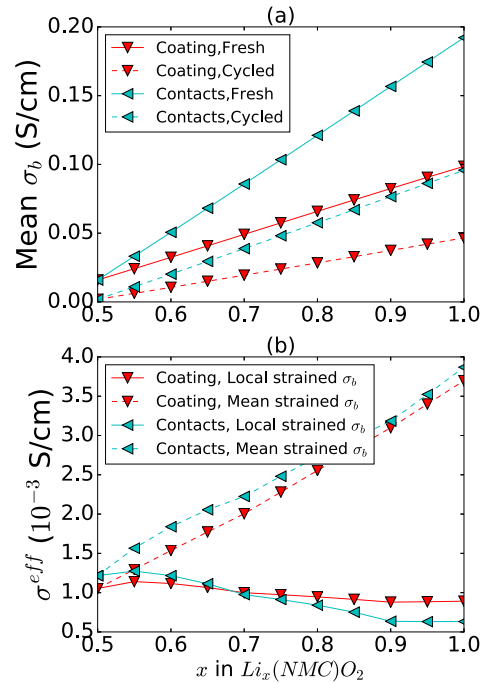


**Figure 19.** (a) Spatial means of composite binder conductivity,  $\sigma_b$ , across lithiation states and (b) the resulting  $\sigma^{eff}$  prediction when using a spatial mean as compared to spatially varying strain-dependent  $\sigma_b$ .

process that impacts battery-scale performance, especially at high discharge rates where ions can form a gradient across the cell-sandwich as they travel between electrodes.<sup>18</sup> Therefore, ionic conductivity and/or tortuosity of the pore network is a useful metric that can directly inform battery-scale simulations. Table II presents both ionic conductivity and tortuosity for the four mesostructure representations. Due to its artificially high porosity, the raw mesostructure unsurprisingly shows a significantly reduced prediction of tortuosity. Interestingly, despite having the same porosity, the contacts mesostructure exhibits a significantly higher tortuosity than the coating and expanded cases, due to its preferential placement of binder near particle contacts, which effectively blocks ionic transport through gaps between particles.

**Thermal conductivity.**—Effective thermal conductivity of the composite cathode is a measurement that is utilized by many macroscale battery modeling efforts<sup>2</sup> and affects how well heat dissipates and transports to the battery boundaries during operation. Effective thermal conductivity values for the four mesostructures are presented in Table II. Since intrinsic thermal conductivity values of composite binder and electrolyte are similar, neglecting binder (raw) and differences in binder location (coating vs. contacts) has a negligible effect on effective thermal transport. In contrast, the expanded case shows significantly higher prediction of effective thermal conductivity, due to the replacement of composite binder/electrolyte with higher thermal conductivity active material. We observe a ~50% increase in effective conductivity although the active material volume increases

**Table II.** Relative effective ionic conductivity, corresponding tortuosity, and effective thermal conductivity for each mesostructure representation.

	$\kappa^{eff}/\kappa_e$	$\tau$	$\kappa^{eff}$
Raw	0.394	1.36	0.701
Expanded	0.285	1.55	1.09
Coating	0.271	1.60	0.731
Contacts	0.238	1.83	0.734

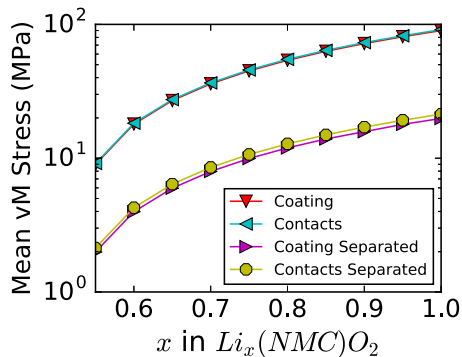


**Figure 20.** Mean von Mises stress for the two binder representations, including cases where particles are separated by a composite binder layer.

just  $\sim 20\%$ . As with the electrical conductivity results, this is due to the creation of many high thermal conductivity pathways through the domain. By expanding neighboring particles slightly, they come into contact and thus a conduction pathway is able to largely bypass low conductivity binder/electrolyte, significantly increasing effective conductivity.

**Separating particles with composite binder.**—As visualized in Figure 9, we consider an additional set of mesostructure cases where all touching particles are separated by a 190 nm composite binder interface layer. The approach replaces any particle-particle contact area with particle-binder area, increasing the latter by 3.3%. This approach yields very minor changes in the effective transport properties discussed previously, but does have a significant effect on the stresses generated within the mesostructure. Figure 20 compares the coating and contacts mesostructure cases to their counterpart versions where an interface binder layer is inserted. Even a small layer of the relatively compliant composite binder reduces stresses by a factor of  $\sim 4.5\times$ , hinting that the composite binder may play a large role in mitigating swelling-induced stress by providing a cushion between particles. Unfortunately, if the composite binder does reside between all particle-particle contacts as we suspect, the significant uncertainty in its size would likely have a significant impact on stress predictions.

## Conclusions

In this paper, we presented several methods that can be used to generate computational meshes from tomography-based composite electrode image stacks with a focus on accounting for the inability to distinguish between non-active phases in the images. We presented three approaches to achieve the correct electrode porosity from binarized active/non-active images: expanding each active particle, applying a uniform composite binder coating on the particles, and a novel approach where binder is preferentially placed near particle contacts in a way that resembles more detailed imaging results in the literature.<sup>57,58</sup> The binder placement techniques presented here can be applied to many types of composite electrodes where active material and binder are mixed into a slurry and then dried ( $\text{LiCoO}_2$ ,  $\text{LiFePO}_4$ , graphite, etc.). We used finite element method simulations to solve both mechanics and transport governing equations in order to extract electrode-scale effective transport properties from the various mesostructure representations. Within these simulations, we consider the lithiation-dependent mechanical swelling and intrinsic electrical conductivity exhibited by the NMC material as well as strain-dependent composite binder electrical conductivity.

Our mesh generation process is unique in that we can include a very large (1000+) number of individual particles and reconstruct a real electrode mesostructure, rather than using isolated particles or synthetic particle geometries. Identifying individual particles al-

lows us to determine particle-particle contact regions and apply our novel composite binder placement algorithm to yield mesostructures that align well with imaging studies by placing composite binder near those regions in a pendular ring shape. This allows us to compare approximations in binder placement and determine if a simple binder coating significantly deviates from a more complex approach. Additionally, we have the ability to separate the particles with a thin interface layer of composite binder, which may be more representative but invisible due to imaging resolution limitations. While previous work has considered isotropic particle swelling within a reconstructed electrode mesostructure,<sup>38</sup> this is the first study that couples the resulting mechanical strain with electrical conductivity simulation by incorporating recently published evidence of composite binder strain-dependent conduction behavior.<sup>79</sup>

We observe a  $2\times$  increase in mean stresses if the particles are simply expanded, due to increased particle-particle contact. When a thin interface layer of binder is forced between particles appearing to be in contact, mean stresses are reduced by  $4.5\times$ , indicating that composite binder may play a large role in lithiation-induced stress mitigation. As NMC lithiation increases, there is an interplay between decreasing NMC electrical conductivity and increasing composite binder electrical conductivity as the binder is compressively strained by swelling NMC particles. Depending on the condition (fresh vs. cycled) of composite binder and conductivity magnitudes considered, this interplay has differing impact on the effective electrical conductivity of the composite cathode. In some cases, effective conductivity is relatively insensitive to lithiation as these two competing phenomena offset. We observe that the uniform binder coating mesostructure exhibits a significantly higher prediction of effective electrical conductivity due to its ability to conduct electricity across the entire domain without conducting through the NMC phase, while preferentially placing binder near particle-particle contact regions forces some conduction through the NMC particles. Therefore, we conclude that a more complex binder representation is necessary for accurate electrode-scale property prediction. Independent of binder placement, not accounting for the strain-dependence of the composite binder results in up to a 50% decrease in effective conductivity predictions, indicating that it is an important material property to incorporate in future simulation efforts. Lastly, we observe that binder coatings and particle expansions underpredict electrolyte tortuosity when compared to the binder-near-contacts approach, which could affect battery-scale simulations, especially at high charge/discharge rates. The algorithm placing composite binder near particle contacts and gaps best matches experimental imaging<sup>57</sup> and these results lead us to the conclusion that this type of preferential placement has a large effect on property prediction and is therefore necessary for future simulation efforts.

Comparisons to related numerical studies may help to validate our results. This same NMC electrode data was used by Vadakkepat et al.<sup>49</sup> for an in-depth investigation of electrode effective thermal conductivity, and  $k^{eff}$  values presented there agree with our values of 0.70–0.73 W/m·K for the non-expanded cases. The reported tortuosity value of 1.39 ( $\chi_{NA} \sim = 0.72$ , neglecting binder) for this electrode matches very well with our value of 1.36 for the raw particles reconstruction. While not directly comparable due to the use of significantly differing intrinsic composite binder conductivities, effective electrical conductivity values in Ref. 51 are consistent with the ranges predicted here in that they are significantly less than 1 S/m for their model at our composite binder pore space percentage of 23%. Tortuosity values of 2.75–3.25 are suggested, which is significantly higher than even our most tortuous result of  $\tau = 1.83$  in the contacts mesostructure. Lastly, Mistry et al.<sup>44</sup> calculated an effective electrical conductivity of 0.001 S/cm for a stochastic mesostructure composed of 95 wt% active material and 5% composite binder, which agrees with our Figure 17a.

A study of these properties and phenomena across multiple electrodes with varying composite binder loading percentages and calendaring pressures is a clear avenue for future work. Dependence of

stress generation and effective transport properties as a function of PVDF/carbon black loading and porosity would provide more information to battery-scale models that may wish to study long-range effects of varying such parameters. Additionally, we plan to consider recent evidence indicating that composite binder material is nanoporous and exhibits significantly reduced but measurable ionic conductivity once wetted with electrolyte.<sup>47,60</sup> Comparisons between mesoscale behavior of various active materials (NMC vs. LCO) or between fresh vs. electrochemically cycled electrode geometries is another candidate for future work, again allowing battery-scale simulations to more accurately account for mesoscale phenomena across a wide parameter space.

### Acknowledgments

The authors would like to thank Anne Grillet for providing the detailed raw data used to construct the strain-dependent composite binder conductivity relationships. We also appreciate Vanessa Wood's group at ETH Zurich for publishing their experimental mesostructure image stacks on their website. We thank Anne Grillet and Dan Bolintineanu for their helpful peer review of this paper. This work was funded by the U.S. Department of Energy (DOE) Vehicle Technologies Office CAEBAT program led by Brian Cunningham at DOE and John Turner at Oak Ridge National Laboratory as a part of the Consortium for Advanced Battery Simulation (CABS). Many of the underlying capabilities utilized in this work were developed as part of Sandia's Laboratory Directed Research and Development Program Battery Degradation project. We thank that team, including Christopher Apblett, Kevin Long, and many others, for many helpful and informative discussions. Sandia National Laboratories is a multi-mission laboratory managed and operated by National Technology and Engineering Solutions of Sandia, LLC, a wholly owned subsidiary of Honeywell International, Inc., for the U.S. Department of Energy's National Nuclear Security Administration under contract DE-NA0003525.

### References

- S. Abada, G. Marlair, A. Lecocq, M. Petit, V. Sauvant-Moynot, and F. Huet, *Journal of Power Sources*, **306**, 178 (2016).
- S. Allu, S. Kalnaus, W. Elwasif, S. Simunovic, J. A. Turner, and S. Pannala, *Journal of Power Sources*, **246**, 876 (2014).
- J. Turner, S. Allu, M. Merrill, W. Elwasif, S. Kalnaus, A. Kumar, D. Lebrun-Grandie, S. Pannala, and S. Simunovic, *Procedia Computer Science*, **51**, 1168. International Conference On Computational Science, {ICCS} 2015Computational Science at the Gates of Nature (2015).
- S. Allu, S. Kalnaus, S. Simunovic, J. Nanda, J. Turner, and S. Pannala, *Journal of Power Sources*, **325**, 42 (2016).
- H. Xie, Q. Zhang, H. Song, B. Shi, and Y. Kang, *Journal of Power Sources*, **342**, 896 (2017).
- D. J. Miller, C. Proff, J. G. Wen, D. P. Abraham, and J. Bareo, *Advanced Energy Materials*, **3**(8), 1098 (2013).
- M. Ebner, F. Marone, M. Stampanoni, and V. Wood, *Science*, **342**(6159), 716 (2013).
- K. Takahashi, K. Higa, S. Mair, M. Chintapalli, N. Balsara, and V. Srinivasan, *Journal of The Electrochemical Society*, **163**(3), A385 (2016).
- C.-F. Chen, P. Barai, K. Smith, and P. P. Mukherjee, *Electrochimica Acta*, **204**, 31 (2016).
- M. Börner, F. Horsthemke, F. Kollmer, S. Haseloff, A. Friesen, P. Niehoff, S. Nowak, M. Winter, and F. Schappacher, *Journal of Power Sources*, **335**, 45 (2016).
- R. Xu and K. Zhao, *Journal of Electrochemical Energy Conversion and Storage*, **13**(3), 030803 (2016).
- H. Wang, A. Kumar, S. Simunovic, S. Allu, S. Kalnaus, J. A. Turner, J. C. Helmers, E. T. Rules, C. S. Winchester, and P. Gorney, *Journal of Power Sources*, **341**, 156 (2017).
- H. Wang, E. Lara-Curzio, E. T. Rule, and C. S. Winchester, *Journal of Power Sources*, **342**, 913 (2017).
- T. F. Fuller, M. Doyle, and J. Newman, *Journal of The Electrochemical Society*, **141**(1), 1 (1994).
- W. B. Gu and C. Y. Wang, *Journal of The Electrochemical Society*, **147**(8), 2910 (2000).
- G. M. Goldin, A. M. Colclasure, A. H. Wiedemann, and R. J. Kee, *Electrochimica Acta*, **64**, 118 (2012).
- E. K. Rahani and V. B. Shenoy, *Journal of The Electrochemical Society*, **160**(8), A1153 (2013).
- B. L. Trembacki, A. Vadakkepatt, S. R. Mathur, and J. Y. Murthy, In *ASME 2013 International Mechanical Engineering Congress and Exposition*, volume 6A (2013).
- M. Wang, X. Xiao, and X. Huang, *Journal of Power Sources*, **348**, 66 (2017).
- B. Yan, C. Lim, L. Yin, and L. Zhu, *Journal of The Electrochemical Society*, **159**(10), A1604 (2012).
- T. Hutzlenbaub, S. Thiele, R. Zengerle, and C. Ziegler, *Electrochemical and Solid-State Letters*, **15**(3), A33 (2012).
- Z. Liu, Y.-C. K. Chen-Wiegart, J. Wang, S. A. Barnett, and K. T. Faber, *Microscopy and Microanalysis*, **22**, 140 (2016).
- M. Ebner, F. Geldmacher, F. Marone, M. Stampanoni, and V. Wood, *Advanced Energy Materials*, **3**(7), 845 (2013).
- S. K. Babu, A. I. Mohamed, J. F. Whitacre, and S. Litster, *Journal of Power Sources*, **283**, 314 (2015).
- A. Etienne, A. Tranchot, T. Douillard, H. Idrissi, E. Maire, and L. Rou, *Journal of The Electrochemical Society*, **163**(8), A1550 (2016).
- M. F. Lagadec, M. Ebner, R. Zahn, and V. Wood, *Journal of The Electrochemical Society*, **163**(6), A992 (2016).
- E. L. Reinholz, S. A. Roberts, C. A. Apblett, J. B. Lechman, and P. R. Schunk, *Journal of The Electrochemical Society*, **163**(8), A1723 (2016).
- O. O. Taiwo, D. P. Finegan, J. Gelb, C. Holzner, D. J. Brett, and P. R. Shearing, *Chemical Engineering Science*, pp. – (2016).
- P. R. Shearing, *Nature Energy*, **1**, 16173 (2016).
- M. Biton, Y. Yufit, F. Tariq, M. Kishimoto, and N. Brandon, *Journal of The Electrochemical Society*, **164**(1), A6032 (2017).
- O. O. Taiwo, J. M. Paz-García, S. A. Hall, T. M. Heenan, D. P. Finegan, R. Mokso, P. Villanueva-Pérez, A. Patera, D. J. Brett, and P. R. Shearing, *Journal of Power Sources*, **342**, 904 (2017).
- H. Kang, C. Lim, T. Li, Y. Fu, B. Yan, N. Houston, V. D. Andrade, F. D. Carlo, and L. Zhu, *Electrochimica Acta*, **232**, 431 (2017).
- C. Lim, B. Yan, L. Yin, and L. Zhu, *Electrochimica Acta*, **75**(0), 279 (2012).
- A. H. Wiedemann, G. M. Goldin, S. A. Barnett, H. Zhu, and R. J. Kee, *Electrochimica Acta*, **88**(0), 580 (2013).
- G. B. Less, J. H. Seo, S. Han, A. M. Sastry, J. Zausch, A. Latz, S. Schmidt, C. Wieser, D. Kehrwald, and S. Fell, *Journal of The Electrochemical Society*, **159**(6), A697 (2012).
- T. Hutzlenbaub, S. Thiele, N. Paust, R. Spotnitz, R. Zengerle, and C. Walchshofer, *Electrochimica Acta*, **115**(0), 131 (2014).
- A. G. Kashkooli, S. Farhad, D. U. Lee, K. Feng, S. Litster, S. K. Babu, L. Zhu, and Z. Chen, *Journal of Power Sources*, **307**, 496 (2016).
- S. A. Roberts, V. E. Brunini, K. N. Long, and A. M. Grillet, *Journal of The Electrochemical Society*, **161**(11), F3052 (2014).
- H. Mendoza, S. A. Roberts, V. E. Brunini, and A. M. Grillet, *Electrochimica Acta*, **190**, 1 (2016).
- S. Lee, A. M. Sastry, and J. Park, *Journal of Power Sources*, **315**, 96 (2016).
- L. Wu, X. Xiao, Y. Wen, and J. Zhang, *Journal of Power Sources*, **336**, 8 (2016).
- K. Higa, S.-L. Wu, D. Y. Parkinson, Y. Fu, S. Ferreira, V. Battaglia, and V. Srinivasan, *Journal of The Electrochemical Society*, **164**(11), E3473 (2017).
- G. Inoue and M. Kawase, *Journal of Power Sources*, **342**, 476 (2017).
- A. Mistri, D. Juarez-Robles, M. Stein, K. Smith, and P. P. Mukherjee, *Journal of Electrochemical Energy Conversion and Storage*, **13**(3), 031006 (2016).
- M. Ebner and V. Wood, *Journal of The Electrochemical Society*, **162**(2), A3064 (2015).
- A. G. Kashkooli, A. Amirfazli, S. Farhad, D. U. Lee, S. Felicelli, H. W. Park, K. Feng, V. De Andrade, and Z. Chen, *Journal of Applied Electrochemistry*, **1** (2017).
- L. Zielke, T. Hutzlenbaub, D. R. Wheeler, C.-W. Chao, I. Manke, A. Hilger, N. Paust, R. Zengerle, and S. Thiele, *Advanced Energy Materials*, **5**(5), 1401612 (2015).
- T. Kanit, S. Forest, I. Galliet, V. Mounoury, and D. Jeulin, *International Journal of Solids and Structures*, **40**(134), 3647 (2003).
- A. Vadakkepatt, B. Trembacki, S. R. Mathur, and J. Y. Murthy, *Journal of the Electrochemical Society*, **163**(2), A1 (2016).
- C. Lim, B. Yan, H. Kang, Z. Song, W. C. Lee, V. De Andrade, F. De Carlo, L. Yin, Y. Kim, and L. Zhu, *Journal of Power Sources*, **328**, 46 (2016).
- L. Zielke, T. Hutzlenbaub, D. R. Wheeler, I. Manke, T. Arlt, N. Paust, R. Zengerle, and S. Thiele, *Advanced Energy Materials*, **4**(8) (2014).
- J. Foster, X. Huang, M. Jiang, S. Chapman, B. Protas, and G. Richardson, *Journal of Power Sources*, **350**, 140 (2017).
- W. Wu, X. Xiao, M. Wang, and X. Huang, *Journal of The Electrochemical Society*, **161**(5), A803 (2014).
- G. Singh and T. K. Bhandakkar, *Journal of The Electrochemical Society*, **164**(4), A608 (2017).
- H. Liu, J. M. Foster, A. Gully, S. Krachkovskiy, M. Jiang, Y. Wu, X. Yang, B. Protas, G. R. Goward, and G. A. Botton, *Journal of Power Sources*, **306**, 300 (2016).
- Z. Liu, T. W. Verhallen, D. P. Singh, H. Wang, M. Wagemaker, and S. Barnett, *Journal of Power Sources*, **324**, 358 (2016).
- S. Jaiser, J. Kumberg, J. Klaver, J. L. Urai, W. Schabel, J. Schmatz, and P. Scharfer, *Journal of Power Sources*, **345**, 97 (2017).
- S. Lim, S. Kim, K. H. Ahn, and S. J. Lee, *Journal of Power Sources*, **299**, 221 (2015).
- M. Müller, L. Pfäffmann, S. Jaiser, M. Baunach, V. Trouillet, F. Scheiba, P. Scharfer, W. Schabel, and W. Bauer, *Journal of Power Sources*, **340**, 1 (2017).
- S. Vierrath, L. Zielke, R. Moroni, A. Mondon, D. R. Wheeler, R. Zengerle, and S. Thiele, *Electrochemistry Communications*, **60**, 176 (2015).
- I. V. Thorat, E. D. Stephenson, N. A. Zacharias, K. Zaghib, J. N. Harb, and D. R. Wheeler, *Journal of Power Sources*, **188**(2), 592 (2009).
- D. Kehrwald, P. R. Shearing, N. P. Brandon, P. K. Sinha, and S. J. Harris, *Journal of The Electrochemical Society*, **158**(12), A1393 (2011).
- H. Wang, Y.-I. Jang, B. Huang, D. R. Sadoway, and Y.-M. Chiang, *Journal of the Electrochemical Society*, **146**(2), 473 (1999).

64. J. Cannarella and C. B. Arnold, *Journal of Power Sources*, **245**(0), 745 (2014).
65. A. R. Denton and N. W. Ashcroft, *Phys. Rev. A*, **43**, 3161 (1991).
66. V. Malavé, J. R. Berger, H. Zhu, and R. J. Kee, *Electrochimica Acta*, **130**(0), 707 (2014).
67. X. Zhang, A. M. Sastry, and W. Shyy, *Journal of The Electrochemical Society*, **155**(7), A542 (2008).
68. L. Chen, X. Xie, J. Xie, K. Wang, and J. Yang, *Journal of Applied Electrochemistry*, **36**(10), 1099 (2006).
69. A. Santimetaneedol, R. Tripuraneni, S. A. Chester, and S. P. Nadimpalli, *Journal of Power Sources*, **332**, 118 (2016).
70. M. Zhu, J. Park, and A. M. Sastry, *Journal of The Electrochemical Society*, **159**(4), A492 (2012).
71. SIERRA Thermal/Fluid Development Team. SIERRA Multimechanics Module: Aria user manual - Version 4.40. Technical Report SAND2016-4159, Sandia National Laboratories (2016).
72. D. R. Noble, E. P. Newren, and J. B. Lechman, *International Journal for Numerical Methods in Fluids*, **63**(6), 725 (2010).
73. R. M. J. Kramer and D. R. Noble, *International Journal for Numerical Methods in Engineering*, pp. n/a–n/a (2014).
74. S. Jaiser, M. Müller, M. Baunach, W. Bauer, P. Scharfer, and W. Schabel, *Journal of Power Sources*, **318**, 210 (2016).
75. R. Amin and Y.-M. Chiang, *Journal of The Electrochemical Society*, **163**(8), A1512 (2016).
76. K. C. Kam, A. Mehta, J. T. Heron, and M. M. Doeff, *Journal of The Electrochemical Society*, **159**(8), A1383 (2012).
77. J. N. Reimers and J. R. Dahn, *Journal of The Electrochemical Society*, **139**(8), 2091 (1992).
78. Z. Chen, L. Christensen, and J. R. Dahn, *Journal of Applied Polymer Science*, **91**(5), 2958 (2004).
79. A. M. Grillet, T. Humplik, E. K. Stirrup, S. A. Roberts, D. A. Barringer, C. M. Snyder, M. R. Janvrin, and C. A. Apblett, *Journal of The Electrochemical Society*, **163**(9), A1859 (2016).
80. G. Liu, H. Zheng, S. Kim, Y. Deng, A. M. Minor, X. Song, and V. S. Battaglia, *Journal of The Electrochemical Society*, **155**(12), A887 (2008).
81. D. Guy, B. Lestriez, R. Bouchet, and D. Guyomard, *Journal of The Electrochemical Society*, **153**(4), A679 (2006).
82. K. Takahata and I. Terasaki, *Japanese Journal of Applied Physics*, **41**(2R), 763 (2002).
83. M. Doyle, J. Newman, A. S. Gozdz, C. N. Schmutz, and J. Tarascon, *Journal of The Electrochemical Society*, **143**(6), 1890 (1996).
84. G. Krishna Bama, P. Indra Devi, and K. Ramachandran, *Journal of Materials Science*, **44**(5), 1302 (2009).
85. P. E. Khizhnyak, A. V. Chechetkin, and A. P. Glybin, *Journal of engineering physics*, **37**(3), 1073 (1979).
86. X. Jin, J. Wu, Z. Liu, and J. Pan, *Fluid Phase Equilibria*, **220**(1), 37 (2004).
87. L. S. de Vasconcelos, R. Xu, J. Li, and K. Zhao, *Extreme Mechanics Letters*, 9, Part 3, 495 . Mechanics of Energy Materials (2016).